Shape-shifting structured lattices via multimaterial 4D printing

J. William Boley[a,b,c,1], Wim M. van Rees[b,d,1], Charles Lissandrello[e], Mark N. Horenstein[f], Ryan L. Truby[b,c], Arda Kotikian[b,c], Jennifer A. Lewis[b,c,2], and L. Mahadevan[b,g,h,i,2]

[a]Department of Mechanical Engineering, Boston University, Boston, MA 02215; [b]Paulson School of Engineering and Applied Sciences, Harvard University, Cambridge, MA 02138; [c]Wyss Institute for Biologically Inspired Engineering, Harvard University, Cambridge, MA 02138; [d]Department of Mechanical Engineering, Massachusetts Institute of Technology, Cambridge, MA 02139; [e]Biological Microsystems, Charles Stark Draper Laboratory, Cambridge, MA 02139; [f]Department of Electrical and Computer Engineering, Boston University, Boston, MA 02215; [g]Department of Physics, Harvard University, Cambridge, MA 02138; [h]Department of Organismic and Evolutionary Biology, Harvard University, Cambridge, MA 02138; and [i]Kavli Institute for Nano-bio Science and Technology, Harvard University, Cambridge, MA 02138

Shape-morphing structured materials have the ability to transform a range of applications. However, their design and fabrication remain challenging due to the difficulty of controlling the underlying metric tensor in space and time. Here, we exploit a combination of multiple materials, geometry, and 4-dimensional (4D) printing to create structured heterogeneous lattices that overcome this problem. Our printable inks are composed of elastomeric matrices with tunable cross-link density and anisotropic filler that enable precise control of their elastic modulus (E) and coefficient of thermal expansion (α). The inks are printed in the form of lattices with curved bilayer ribs whose geometry is individually programmed to achieve local control over the metric tensor. For independent control of extrinsic curvature, we created multiplexed bilayer ribs composed of 4 materials, which enables us to encode a wide range of 3-dimensional (3D) shape changes in response to temperature. As exemplars, we designed and printed planar lattices that morph into frequency-shifting antennae and a human face, demonstrating functionality and geometric complexity, respectively. Our inverse geometric design and multimaterial 4D printing method can be readily extended to other stimuli-responsive materials and different 2-dimensional (2D) and 3D cell designs to create scalable, reversible, shape-shifting structures with unprecedented complexity.

4D printing | shape shifting | multimaterial

Shape-morphing structured systems are increasingly seen in a range of applications from deployable systems (1, 2) and dynamic optics (3, 4) to soft robotics (5, 6) and frequency-shifting antennae (7), and they have led to numerous advances in their design and fabrication using various 3-dimensional (3D) and 4-dimensional (4D) printing techniques (8, 9). However, to truly unleash the potential of these methods, we need to be able to program arbitrary shapes in 3 dimensions (i.e., control the metric tensor at every point in space and time), thus defining how lengths and angles change everywhere. For thin sheets, with in-plane dimensions that are much larger than the thickness, this is mathematically equivalent to specifying the first and second fundamental forms of the middle surface. These quadratic forms describe the relation between material points in the tangent plane and the embedding of the middle surface in 3 dimensions and thus, control both the intrinsic and extrinsic curvature of the resulting surface (10, 11). From a physical perspective, arbitrary control of the shape of a sheet requires the design of material systems that can expand or contract in response to stimuli, such as temperature, humidity, pH, etc., with the capacity to generate and control large in-plane growth gradients combined with differential growth through the sheet thickness (12, 13). Such systems are difficult to achieve experimentally; hence, most current shape-shifting structures solutions rarely offer independent control of mean and Gaussian curvatures (14, 15). We address this challenge by 4D printing a lattice design composed of multiple materials.

Beginning at the material level, we created printable inks based on a poly(dimethylsiloxane) (PDMS) matrix, an elastomeric thermoset

that exhibits a large operating temperature window and a high thermal expansion coefficient (16). Although the inks are printed at room temperature, the broad range of polymerization temperatures for PDMS enables us to cure the resulting structures at much higher temperatures. On cooling to room temperature, these cured matrices achieve maximal contraction, hence transforming into their deployed states. The same base elastomer is used in all inks to facilitate molecular bonding between adjacent ribs and layers. To create inks with reduced thermal expansivity, we fill the elastomer matrix with short glass fibers (20% wt/wt) that preferentially shear align along the print path (Fig. 1 *A–C*) (8, 17). To impart rheological properties suitable for direct ink writing (i.e., a shear yield stress, shear thinning response, and plateau storage modulus) (*SI Appendix*, Fig. S1), we add fumed silica (20 to 22% wt/wt) (*SI Appendix*) to these ink formulations. As an added means of tuning their coefficient of thermal expansion

Significance

Thin shape-shifting structures are often limited in their ability to morph into complex and doubly curved shapes. Such transformations require both large in-plane expansion or contraction gradients and control over extrinsic curvature, which are hard to achieve with single materials arranged in simple architectures. We solve this problem by 4-dimensional printing of multiple materials in heterogeneous lattice designs. Our material system provides a platform that achieves in-plane growth and out-of-plane curvature control for 4-material bilayer ribs. The lattice design converts this into large growth gradients, which lead to complex, predictable 3-dimensional (3D) shape changes. We demonstrate this approach with a hemispherical antenna that shifts resonant frequency as it changes shape and a flat lattice that transforms into a 3D human face.

Fig. 1. Printable elastomeric inks with tailored α and E. (A) Schematic of a multimaterial 4D printing lattice structure, with ribs depicted as being 2 filaments wide and 2 filaments tall. (B) Micrograph of printed fiber-filled filament showing alignment of glass fibers, where $\parallel$ corresponds to the print direction and $\perp$ is perpendicular to the print direction. (C) Resulting alignment probability density from B showing that the glass fibers align with the print direction, where a 0° angle corresponds to $\parallel$. (D) Schematic illustrating varying of x-link to base ratio by weight (x-link:base by weight) for the elastomer matrix. (E) Measured α for different ink formulations as a function of x-link:base by weight. Lines represent linear fits to experimental data of the corresponding color. (F) Measured E of different ink formulations as a function of x-link:base by weight. Lines represent exponential fits to experimental data of corresponding color.

α and their elastic modulus E, we vary the cross-link to base weight ratio (x-link:base by weight) (Fig. 1D and *SI Appendix*) within the elastomeric matrices. Unlike prior work, we generate a palette of 4D printable inks that span a broad range of properties (i.e., α ranges from 32×10^{-6} to 229×10^{-6} 1/°C, while E ranges from 1.5 to 1,245 kPa) (Fig. 1 E and F and *SI Appendix*, Figs. S2 and S3).

To go beyond the geometric limitation associated with uniform isotropic or anisotropic sheets, we used multimaterial 4D printing to first create simple bilayers (*SI Appendix*, Fig. S4A), the basic functional unit of our multiplexed bilayer lattices. The curvature response of these bilayers to a temperature change (ΔT) can be expressed as (18)

$$\frac{\delta \kappa t_2}{\Delta T} = (\alpha_2 - \alpha_1) \frac{6\beta\gamma(1+\beta)}{1 + 4\beta\gamma + 6\beta^2\gamma + 4\beta^3\gamma + \beta^4\gamma^2}, \quad [1]$$

where $\delta \kappa = \kappa - \tilde{\kappa}$ is the change in curvature after ΔT, $\tilde{\kappa}$ is the curvature of the bilayer before ΔT, κ is the curvature after ΔT, t is the layer thickness, $\beta = t_1/t_2$, $\gamma = E_1/E_2$, and subscripts 1 and 2 denote the low and high α materials, respectively. The assumptions underlying this equation relate to the nature of the elastic deformation, material characteristics of the rib, and the cross-sectional shape of the layers, and they are further discussed in *SI Appendix*. We use Eq. 1 to delineate a space of dimensionless curvature increments ($\delta \kappa t_2/\Delta T$) with respect to dimensionless bilayer thickness (t_1/t_2) for different ink combinations, which is in good agreement with the corresponding printed bilayers (*SI Appendix*, Fig. S4B). The curvature change of our experimental bilayers is reversible and repeatable as demonstrated by thermal cycling experiments (*SI Appendix*, Fig. S4C). However, these simple bilayer elements alone do not provide a path to significantly altering the midsurface metric, which is necessary for complex 3D shape changes. For example, the maximum linear in-plane growth that can be achieved with this set of materials, for $\Delta T = \pm 250$ °C, is limited to $\pm 6.4\%$.

To overcome this limitation, we arranged the bilayers into an open cell lattice (19) via multimaterial 4D printing (Fig. 2 A–C).

We consider this lattice a mesoscale approximation of the underlying continuous surface, in which an average metric can now be rescaled with significantly larger growth factors than the largest thermally realizable linear growth of the constituent materials (19, 20). Specifically, if the initial distance between the lattice nodes is denoted $\tilde{L}$ and the initial sweep angle of the ribs is denoted $\tilde{\theta}$, a change in curvature $\delta \kappa$ as computed with Eq. 1 leads to a new distance between lattice nodes L. The linear growth factor, $s = L/\tilde{L}$, of each rib (and hence, of the entire homogeneous isotropic lattice) can be expressed by the following equation:

$$s = \frac{L}{\tilde{L}} = \frac{2 \sin\left(\frac{1}{4}\tilde{\theta}\left(2 + \frac{\tilde{L}\delta\kappa}{\sin(\tilde{\theta}/2)}\right)\right)}{2 \sin\left(\tilde{\theta}/2\right) + \tilde{L}\delta\kappa} \quad [2]$$

(*SI Appendix*). In Fig. 2 B and C, we show 2×2-cell printed lattices of various $\tilde{L}$ and $\tilde{\theta}$, in which ribs undergo a fixed change in curvature ($\delta \kappa \approx 72$ mm^{-1} for $\Delta T = 250$ °C; computed using Eq. 1). The measured linear growth for the different ($\tilde{L}, \tilde{\theta}$) combinations agrees well with Eq. 2 (Fig. 2C) and demonstrates a tremendous range from 79% contraction to 41% expansion. As in the simple bilayer case, these lattices can undergo repeated expansion and contraction in response to a temperature field (Movie S1). Plotting the entire space of growth factors s as a function of $\tilde{\theta}$ (with $-\pi \leq \tilde{\theta} \leq \pi$) and $\tilde{L}\delta\kappa$ (*SI Appendix*, Fig. S5) reveals that, for $\tilde{L}\delta\kappa \geq 2$, it is possible to create ribs that result in $s = 0$ (i.e., with arbitrarily large linear contraction ratios). For the considered lattice design, the upper bound for the opening angle is $|\tilde{\theta}| \leq |\tilde{\theta}_{max}| < \pi$, where $\tilde{\theta}_{max}$ corresponds to the maximum sweeping angle that can be achieved without 2 adjacent ribs touching at their edges so that the minimum value of $\tilde{L}\delta\kappa$ for which $s = 0$ will be slightly larger than 2 in reality (*SI Appendix*).

While this homogeneous lattice design can achieve an isotropic rescaling of the Euclidean metric, inducing intrinsic (Gaussian) curvature in an initially planar sheet requires spatial gradients of
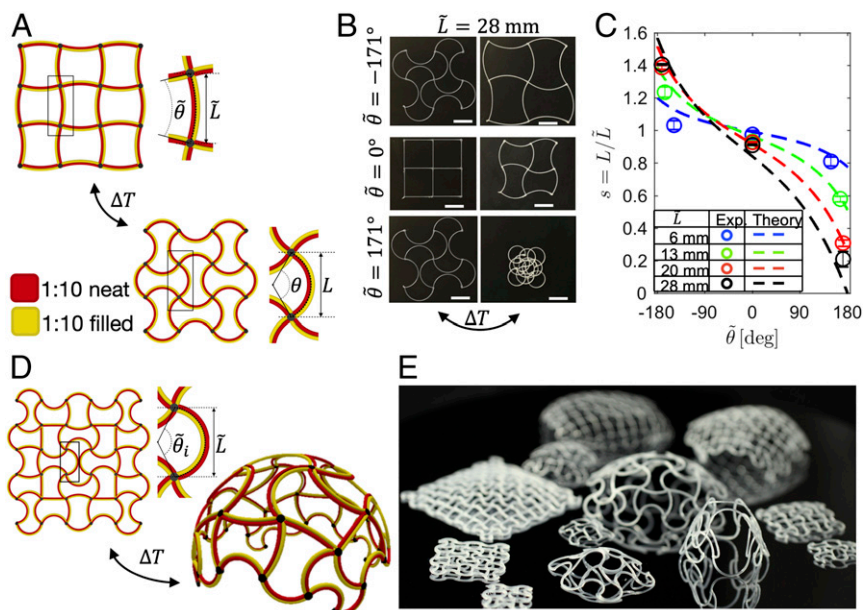
Fig. 2. Multimaterial 4D printing of homogeneous and heterogeneous lattices. (*A*) Schematic of bilayer lattice with defined parameters: printed lattice spacing ($\tilde{L}$) and arc angle ($\tilde{\theta}$) and morphed lattice spacing (L) and arc angle (θ) after applied temperature field (ΔT). (*B*) Images of 2D lattices as printed (*Left*) and after applying a ΔT of −250 °C (*Right*). (Scale bar, 20 mm.) (*C*) Linear growth factor of various printed lattices and their comparison with theory (Eq. **2**) after applying a ΔT of −250 °C. (*D*) Schematic of a 2D heterogeneous lattice design that morphs into a spherical cap under an applied ΔT. (*E*) Photograph of various printed lattices after morphing into spherical caps.

the metric tensor along the surface. To achieve this, we used a heterogeneous lattice in which the initial sweep angle of every rib is considered an independent degree of freedom and is, therefore, indexed within the lattice (Fig. 2*D*). From a conformal map of the desired target shape to the plane, we can compute the required growth factor for each rib and invert Eq. **2** to find the corresponding value of θ_i (*SI Appendix*). With this approach, we theoretically show the maximum possible opening angle of a grown spherical cap as a function of $\tilde{L}\delta\kappa$ in *SI Appendix*, Fig. S6, demonstrating the theoretical capability of this approach to create a flat lattice that can morph into a complete sphere when $\tilde{L}\delta\kappa \geq 2$ (assuming the idealized case where $\theta_{\max} = \pi$ for simplicity) (*SI Appendix*). We test the efficacy of this approach by transforming flat, square lattices into freestanding spherical caps (Fig. 2 *D* and *E* and *SI Appendix*, Fig. S7) and saddles (*SI Appendix*, Fig. S8). As a preview of multishape possibilities (polymorphism), we leveraged the fact that these PDMS matrices swell when exposed to a variety of solvents (21). We show that a planar lattice programmed to transform into a spherical cap (positive Gaussian curvature) through a negative temperature change can also be transformed beyond its printed configuration to adopt a saddle-shaped geometry (negative Gaussian curvature) when immersed in a solvent (*SI Appendix*, Fig. S9 and Movie S2). Using multimaterial 4D printing, we produced different spherical caps by parametrically varying the number of printed filaments along the width and height of the lattice ribs (N_w and N_h, respectively), the number of cells along either direction of the lattice ($N_x = N_y = N$), and $\tilde{L}$. One factor affecting these freestanding lattices is their ability to support their own weight without sagging (*SI Appendix*, Fig. S7A). At a scaling level, the nondimensional sagging deflection d_s may be written as

$$\frac{d_s}{\tilde{L}} \sim \left(\frac{\overline{\rho}g}{\overline{E}}\right)\left(\frac{(N\tilde{L})^3}{h^2}\right),\qquad[3]$$

with $\overline{\rho}$ being the average rib density, g being gravity, h being the rib height, and $\overline{E}$ being the average elastic modulus of a rib (*SI*

Appendix). Our experiments confirm that sagging lattices (i.e., when $d_s/\tilde{L}$ is large) also have large values of $\left(\frac{\overline{\rho}g}{\overline{E}}\right)\left(\frac{(N\tilde{L})^3}{h^2}\right)$, but the lattice remains relatively undeformed when $\left(\frac{\overline{\rho}g}{\overline{E}}\right)\left(\frac{(N\tilde{L})^3}{h^2}\right)$ becomes sufficiently small (*SI Appendix*, Fig. S7A and Table S1). For the nonsagging structures ($d_s/\tilde{L} < \sim 10$), the predominant factor affecting their shape transformation is the extent to which the internal α-generated strains can buckle the lattice. We can quantify this by comparing the measured lattice curvature (κ_s) with its theoretical target curvature (κ_t). At a scaling level, the critical strain ϵ_{crit}, above which the lattice is expected to buckle out of plane, is given by (*SI Appendix*)

$$\epsilon_{\text{crit}} \sim \left(\frac{h}{N\tilde{L}}\right)^2.\qquad[4]$$

The experimental lattices that are characterized by large values ϵ_{crit} ($> \sim 6 \times 10^{-4}$) indeed remain flat and do not adopt the curved state (*SI Appendix*, Fig. S7B). However, increasing the slenderness of the ribs by either increasing $N\tilde{L}$ or decreasing h reduces the error compared with the theoretical prediction (*SI Appendix*, Fig. S7B and Table S1) as expected.

To fully control 3D shape requires the ability to program both the intrinsic curvature and extrinsic curvature. We achieved this by introducing multiplexed pairs of bilayers as ribs within heterogeneous lattices that exploit the large range of α and E values exhibited by our ink palette. Specifically, 4 different materials are used in the cross-sections of each rib, which allows us to control expansion across their thickness and width according to Eq. **1**. We can direct normal curvature up or down by interchanging the top and bottom layers and discretely control its magnitude by transposing the materials in the cross-section as shown in Fig. 3.

Altogether, our multiplexed bilayer rib lattice yields a shape-changing structural framework with 2 significant novelties compared with other motifs. First, these lattices exhibit a substantial amount of local linear in-plane growth (40% growth to 79%

Boley et al.

A 4-materials with matching curvature response

B 2x2 material ribs direct the out-of-plane curvature

C Flipping/transposing material combinations provides five levels of control
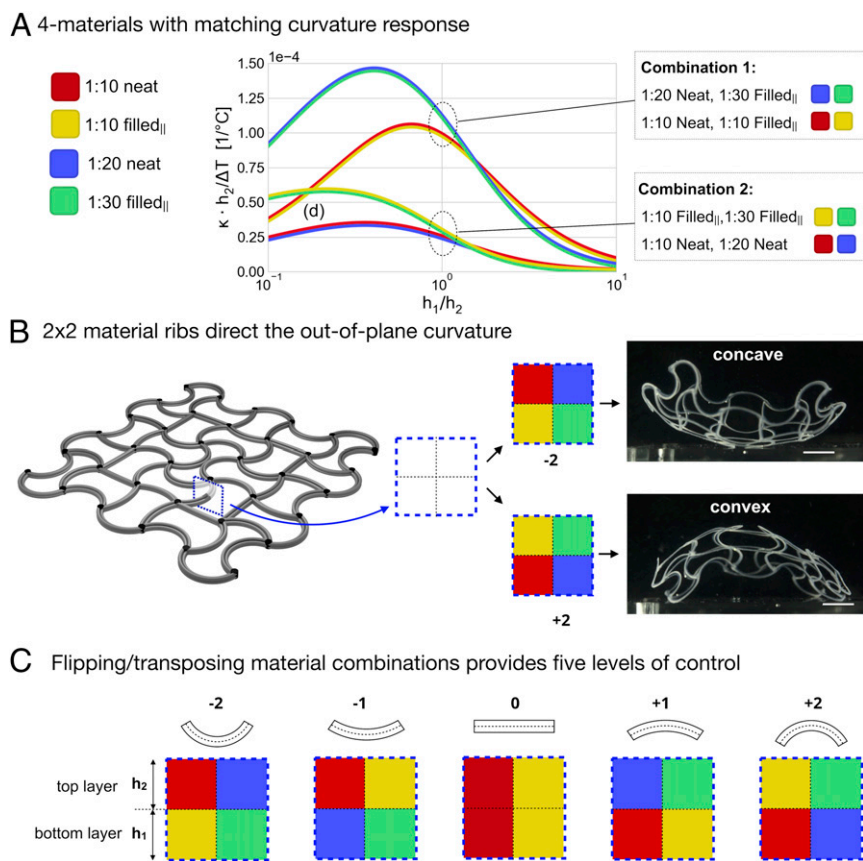
Fig. 3. Multiplex bilayer lattices via multimaterial 4D printing. (*A*) Dimensionless bilayer curvature increments for the 4 different bilayer material combinations. The materials are chosen so that adjacent pairs of equal thicknesses achieve approximately matching curvature increments. While in-plane curvature of each rib is governed by the left–right material pairs and the in-plane opening angle as described in the text and *SI Appendix*, Fig. S5, the out-of-plane curvature of each rib is governed by the top–bottom material pairs according to the graph. (*B*) Schematic of the multiplex bilayer lattice highlighting the cross-section of a rib and 2 experimental examples of 4D printed 4-material hemispherical lattices with maximum concave (*Upper*) and maximum convex (*Lower*) multiplex cross-sections. (Scale bars, 10 mm.) (*C*) Schematics of all possible material combinations for such a cross-section. With 2 materials, the lattice has a symmetric cross-section and 0 mean curvature (labeled 0). Adding 2 more materials enables us to achieve 4 different combinations of out-of-plane curvature ranging from maximum concave (labeled −2) to maximum convex (labeled +2).

contraction as currently demonstrated; 57% times growth to 100% contraction in theory), which can be independently varied across the lattice as well as in each of the 2 orthogonal directions of the lattice. This capability can be generalized to lattices of different scales, materials, and/or stimuli. Second, the out-of-plane bending control reduces elastic frustration, which simplifies their inverse design and expands the range of shapes that can be achieved compared with prior work (8, 22).

To test the capability of our approach to create dynamic functional structures, we innervate these freestanding lattices with liquid metal features composed of a eutectic gallium indium ink that are printed within selected ribs throughout the lattice
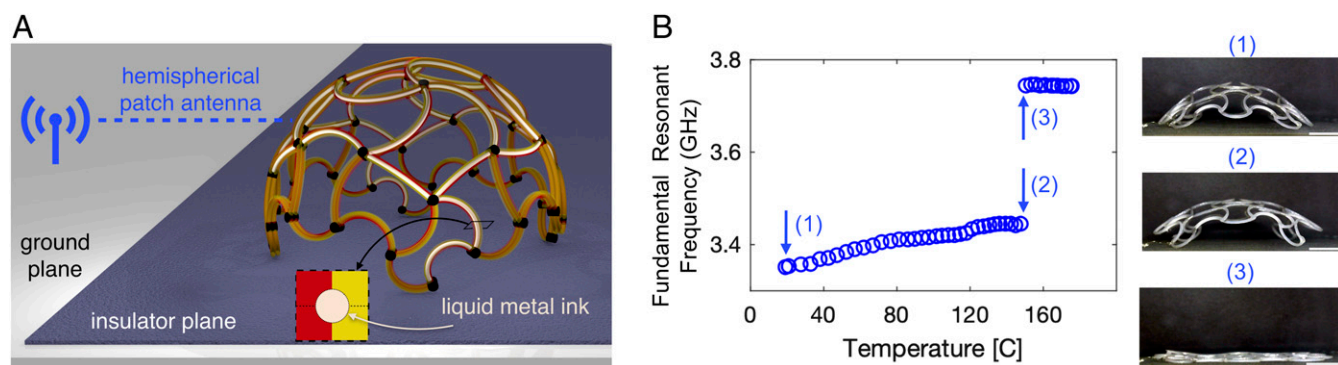
Fig. 4. Shape-shifting patch antenna. (*A*) Schematic of experimental setup for a spherical cap lattice innervated with a liquid metal ink, which is used as a shape-shifting patch antenna. (*B*) Resonant frequency of a printed patch antenna at various temperatures (*Left*) and side view images of the antenna corresponding to different resonant frequencies (*Right*). Parameters for all lattices are as follows: low α material is 1:10 filled$_{\parallel}$, high α material is 1:10 neat, and $t_1 = t_2 = 0.4$ mm. (Scale bars, 10 mm.)

Boley et al.
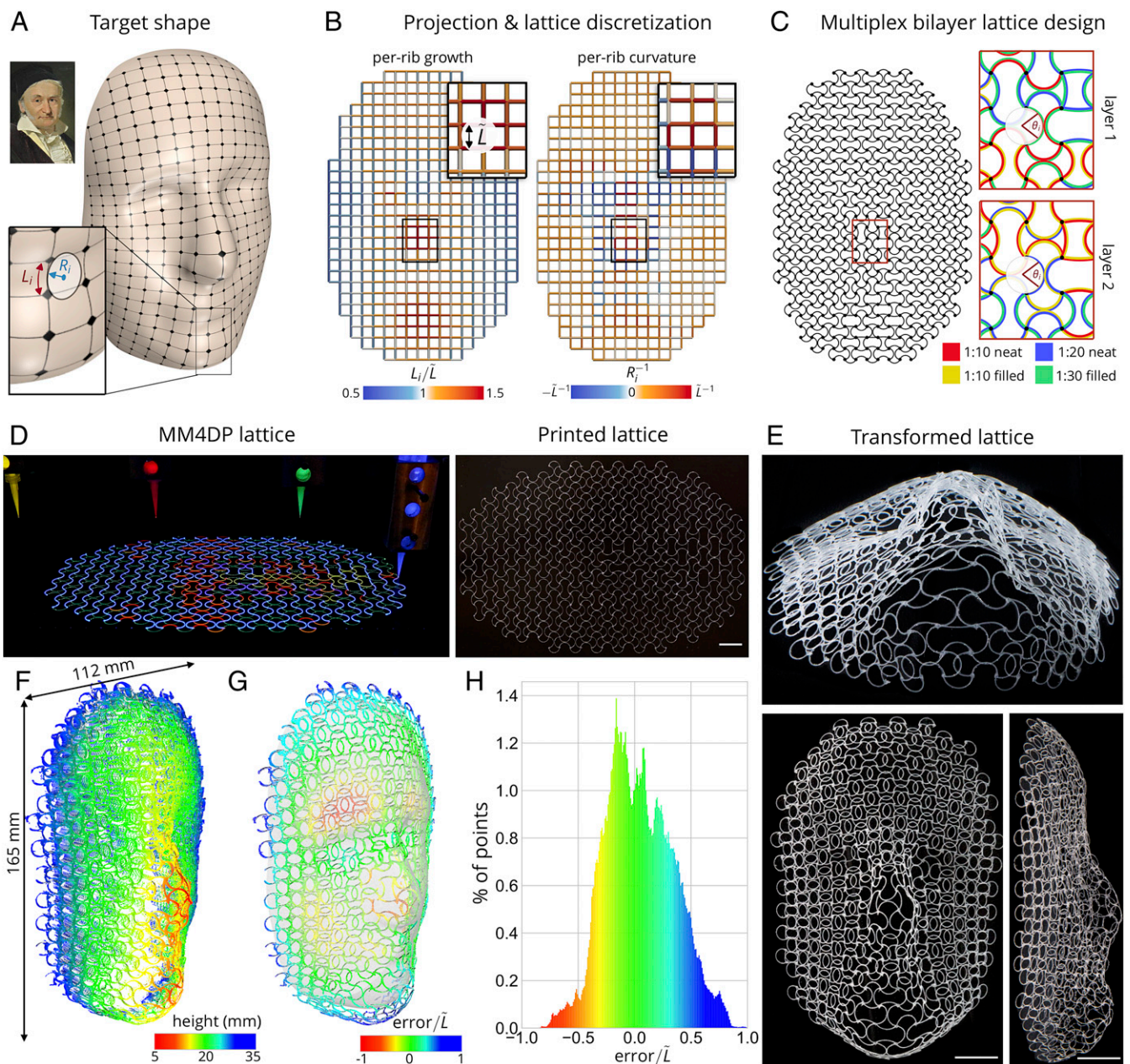
Fig. 5. Integrated design and fabrication of a complex geometrical shape. (*A*) Process for creating a 3D face as the target shape: begin with a 2D image of Carl Friedrich Gauss's likeness (*Upper Left*) and generate a 3D surface (the target shape) via an artificial intelligence algorithm. The detailed view highlights the target length (L_i) and normal radius of curvature (R_i) for 1 specific rib. (*B*) Conformally mapped and discretized lattice with resulting local rib growth ($L_i/\tilde{L}$) and normal curvature (R_i^{-1}), where $\tilde{L} = 10$ mm. (*C*) Programmed multiplex bilayer lattice for printing. Detailed views show a sample area of the programmed lattice, with first and second layers of the lattice showing prescribed $\tilde{\theta}_i$ and multiplex materials. (*D*) Photographs of lattice during (*Left*) and after (*Right*) printing. MM4DP, multimaterial 4D printing. (Note that fluorophores are incorporated in each ink to highlight multimaterial printing.) (Scale bar, 20 mm.) (*E*) Photographs of lattice after transformation. Perspective view (*Upper*), top view (*Lower Left*), and side view (*Lower Right*) of transformed lattice. $\Delta T = -250\,°C$. (Scale bars, 20 mm.) (*F*) A 3D scan of the transformed face. (*G*) Normalized error (error$/\tilde{L}$) of the 3D scan superimposed onto target shape. Negative values represent points that lie below target shape surface. Positive values represent points that lie above target shape surface. (*H*) Distribution of normalized error.

(Fig. 4*A* and *SI Appendix*) to yield a shape-shifting patch electromagnetic antenna (Fig. 4 *A* and *B*). We printed a 2-material lattice ($N_x = N_y = 5, N_w = N_h = 4$) programmed to change shape into a spherical cap when cooled to room temperature after curing at 250 °C. On reheating this structure, we see a gradual increase in the fundamental resonant frequency as its effective height decreases (Fig. 4*B* and Movie S3). This trend continues until the functional lattice reaches a critical temperature of ~150 °C, where internal forces can no longer support its weight or provide

the appropriate out-of-plane buckling force (i.e., it rapidly returns to its flat-printed geometry). As expected, we observe a sharp increase in the fundamental resonant frequency when this transition occurs. While shape-shifting patch antennae are of interest for wireless sensing and dynamic communication, the ability to integrate conductive ribs could be harnessed for other shape-shifting soft electronic and robotic applications.

To test the capability of our approach to create shapes with complex geometrical features on multiple scales, we printed a planar

lattice that transforms into a human face (Fig. 5 and Movies S4 and S5). We chose to create a simulacrum of the face of C. F. Gauss, father of modern geometry, starting with a 3D target surface mesh (Fig. 5*A*) generated from a painting of Gauss through a machine learning algorithm (23) (*SI Appendix*). We conformally project the face to the plane and discretize the planar projection using a lattice with $\tilde{L} = 10$ mm and $N_x \times N_y = 18 \times 27$ cells truncated to the outline of the surface map. After this discretization, we find among all ribs the maximum and minimum required growth factors $s_{max} = 1.42$ and $s_{min} = 0.43$, respectively. The largest growth factors are required near the nose and the chin, where the target mesh has the most substantial Gaussian curvature. We chose ribs with $N_w = N_h = 2$ and generated $\tilde{\theta}_i$ attuned to the required growth by inverting Eq. **2** (*SI Appendix*, Fig. S10). Furthermore, since large parts of the face have almost zero Gaussian curvature, we can rely on our multiplexed bilayer technique to influence the normal curvature independent of the metric transformation (Fig. 5 *B* and *C*). The normal curvature changes sign most prominently near the eye sockets, where the mean curvature undergoes a sign change compared with the rest of the face. With these choices, the lattice dimensionless sagging parameter is $d_s/\tilde{L} \sim \mathcal{O}(10^3)$ (i.e., it cannot support its own weight in air). Immersion of this multimaterial lattice (Fig. 5*D*) in a salt water tank, in which density is only slightly less than the average lattice density (*SI Appendix*), prevents sagging yet allows the lattice to sink to the bottom of the tank (Movie S5). After its shape transformation, the printed lattice shows a clear correspondence to the target geometry (Fig. 5*E*), where the more prominent features of the face, such as the nose, chin, and eye sockets; the finer features associated with the lips and cheeks; and the subtle curvature transitions are all visible. This multiplexed bilayer approach is successful in directing spherical regions up (nose and chin) or down (eye sockets) as required and achieves significant mean curvature near the forehead and around the perimeter of the face, where the Gaussian curvature is small. To test the accuracy of our printed lattice, we obtained a 3D reconstruction of the transformed face (Fig. 5*F*) using a laser-scanning technique (*SI Appendix*). By fitting the scanned data to the target surface (*SI Appendix*), we can compute the smallest distance from each point on the scanned face to the target shape. We use this distance as an error metric and normalize it as error/$\tilde{L}$ (Fig. 5*G*). The distribution of the normalized error (Fig. 5*H*) exhibits a 95% confidence interval within ±0.62, showing the high accuracy of our multimaterial 4D printing method.

The lattice designs described here are applicable to a wide range of materials, length scales, and stimuli. For example, a lattice with ribs of equal widths ($w_1 = w_2 = w$) and elastic modulus ($E_1 = E_2 = E$) can achieve unbounded contraction when the differential strain between the 2 layers is larger than $8w/3\tilde{L}$. The value of $\tilde{L}$ then determines the range of linear growth that can be achieved, but it also dictates the cell size of the lattice and thereby, the scale of the features that can be captured by the deployed lattice. For a given design, this implies that we should minimize $\tilde{L}$ under the constraint that the required linear growth factors can still be achieved with the specified materials and rib geometry. Independent of $\tilde{L}$ and similar to our theoretical work on bilayer sheets (13), we further expect that there exists a constraint on the maximum target shape curvature that is inversely proportional to the thickness of the ribs.

The lattice architecture can be extended to larger scales of freestanding structures by designing materials with similar α and larger E (and/or smaller ρ) so that, to first approximation, the lattice-based structure would still provide the desired metric changes. Moreover, this approach can be applied to smaller microscale structures by utilizing smaller fillers and nozzle diameters. As these lattice architectures are agnostic to the mode of stimulus, one can imagine designing general lattices with local, variable actuation for myriad materials systems and stimuli [e.g., pneumatics (24, 25), light (26), temperature (27), pH (28), solvent (8, 29), electric field (6), or magnetic field (30)] to transform the same lattice reversibly and dynamically into one or multiple complex shapes.

Our inverse design procedure can be broadened not only to include arbitrary geometries of the underlying lattice but also, to multiplexed bilayers with different material compositions, each of which can be independently varied in space. While we have restricted ourselves to conformal maps and square lattice cells here, our method can be generalized for other projections, spatially varying cell sizes, different tessellations of the plane, and other 2-dimensional (2D) and 3D open cell lattice designs (31–33). By using temperature as stimulus, these lattices can be repeatedly and rapidly (as quickly as ∼70ms) (*SI Appendix*, Table S2) actuated in a continuous, well-controlled, and predictable manner. Altogether, our multimaterial 4D printed lattice provides a versatile platform for the integrated design and fabrication of complex shape-morphing architectures for tunable antennae, dynamic optics, soft robotics, and deployable systems that were previously unattainable.

1. K. Saito, S. Nomura, S. Yamamoto, R. Niiyama, Y. Okabe, Investigation of hindwing folding in ladybird beetles by artificial elytron transplantation and microcomputed tomography. *Proc. Natl. Acad. Sci. U.S.A.* **114**, 5624–5628 (2017).

2. M. Mobrem, D. Adams, Lenticular jointed antenna deployment anomaly and resolution onboard the Mars express spacecraft. *J. Spacecr. Rockets* **46**, 403–410 (2009).

3. M. Piovarči, M. Wessely, M. Jagielski Michałand Alexa, W. Matusik, P. Didyk, "Directional screens" in *Proceedings of the 1st Annual ACM Symposium on Computational Fabrication* (Association for Computing Machinery, New York, NY 2017), pp. 1:1–1:10.

4. T. G. Bifano, Microelectromechanical deformable mirrors. *IEEE J. Sel. Top. Quantum Electron.* **5**, 83–89 (1999).

5. M. Wehner *et al.*, An integrated design and fabrication strategy for entirely soft, autonomous robots. *Nature* **536**, 451–455 (2016).

6. E. Acome *et al.*, Hydraulically amplified self-healing electrostatic actuators with muscle-like performance. *Science* **359**, 61–65 (2018).

7. M. Rashed Khan, G. J. Hayes, J. H. So, G. Lazzi, M. D. Dickey, A frequency shifting liquid metal antenna with pressure responsiveness. *Appl. Phys. Lett.* **99**, 013501 (2011).

8. A. S. Gladman, E. A. Matsumoto, R. G. Nuzzo, L. Mahadevan, J. A. Lewis, Biomimetic 4D printing. *Nat. Mater.* **15**, 413–418 (2016).

9. X. Kuang *et al.*, Advances in 4D printing: Materials and applications. *Adv. Funct. Mater.* **29**, 1805290 (2019).

10. K. F. Gauss, *General Investigations of Curved Surfaces* (Princeton University Library, 1902).

11. Y. Klein, E. Efrati, E. Sharon, Shaping of elastic sheets by prescription of non-Euclidean metrics. *Science* **315**, 1116–1120 (2007).

12. G. W. Jones, L. Mahadevan, Optimal control of plates using incompatible strains. *Nonlinearity* **28**, 3153–3174 (2015).

13. W. M. van Rees, E. Vouga, L. Mahadevan, Growth patterns for shape-shifting elastic bilayers. *Proc. Natl. Acad. Sci. U.S.A.* **114**, 11597–11602 (2017).

14. S. J. Jeon, A. W. Hauser, R. C. Hayward, Shape-morphing materials from stimuli-responsive hydrogel hybrids. *Acc. Chem. Res.* **50**, 161–169 (2017).

15. H. Ko, A. Javey, Smart actuators and adhesives for reconfigurable matter. *Acc. Chem. Res.* **50**, 691–702 (2017).

16. B. Matthew *et al.*, *Silicones* (Kirk-Othmer Encyclopedia of Chemical Technology, 2002).

17. B. G. Compton, J. A. Lewis, 3D-printing of lightweight cellular composites. *Adv. Mater.* **26**, 5930–5935 (2014).

18. S. Timoshenko, Analysis of bi-metal thermostats. *J. Opt. Soc. Am.* **11**, 233 (1925).

19. R. Lakes, Cellular solid structures with unbounded thermal expansion. *J. Mater. Sci. Lett.* **15**, 475–477 (1996).

ENGINEERING

20. L. Guiducci et al., Honeycomb actuators inspired by the unfolding of ice plant seed capsules. *PLoS One* **11**, e0163506 (2016).
21. J. N. Lee, C. Park, G. M. Whitesides, Solvent compatibility of poly(dimethylsiloxane)-based microfluidic devices. *Anal. Chem.* **75**, 6544–6554 (2003).
22. H. Aharoni, Y. Xia, X. Zhang, R. D. Kamien, S. Yang, Universal inverse design of surfaces with thin nematic elastomer sheets. *Proc. Natl. Acad. Sci. U.S.A.* **115**, 7206–7211 (2018).
23. A. S. Jackson, A. Bulat, V. Argyriou, G. Tzimiropoulos, "Large pose 3D face re-construction from a single image via direct volumetric CNN regression" in *Proceedings of the IEEE International Conference on Computer Vision and Pattern Recognition* (IEEE, Piscataway, NJ, 2017).
24. R. L. Truby et al., Soft somatosensitive actuators via embedded 3D printing. *Adv. Mater.* **30**, e1706383 (2018).
25. J. H. Pikul et al., Stretchable surfaces with programmable 3D texture morphing for synthetic camouflaging skins. *Science* **358**, 210–214 (2017).
26. S. J. Park et al., Phototactic guidance of a tissue-engineered soft-robotic ray. *Science* **353**, 158–162 (2016).
27. A. Kotikian, R. L. Truby, J. W. Boley, T. J. White, J. A. Lewis, 3D printing of liquid crystal elastomeric actuators with spatially programed nematic order. *Adv. Mater.* **30**, 1706164 (2018).
28. L. D. Zarzar, P. Kim, J. Aizenberg, Bio-inspired design of submerged hydrogel-actuated polymer microstructures operating in response to pH. *Adv. Mater.* **23**, 1442–1446 (2011).
29. J. Kim, J. A. Hanna, M. Byun, C. D. Santangelo, R. C. Hayward, Designing responsive buckled surfaces by halftone gel lithography. *Science* **335**, 1201–1205 (2012).
30. Y. Kim, H. Yuk, R. Zhao, S. A. Chester, X. Zhao, Printing ferromagnetic domains for untethered fast-transforming soft materials. *Nature* **558**, 274–279 (2018).
31. O. Sigmund, S. Torquato, Composites with extremal thermal expansion coefficients. *Appl. Phys. Lett.* **69**, 3203–3205 (1996).
32. R. Lakes, Cellular solids with tunable positive or negative thermal expansion of unbounded magnitude. *Appl. Phys. Lett.* **90**, 221905 (2007).
33. H. Zhu, T. Fan, Q. Peng, D. Zhang, Giant thermal expansion in 2D and 3D cellular materials. *Adv. Mater.* **30**, e1705048 (2018).